Extensions of the meshless Finite Volume Particle Method (FVPM) for static and dynamic free-surface flows

Nathan J. Quinlan*

Mechanical Engineering, National University of Ireland Galway.

Abstract

The Finite Volume Particle Method (FVPM) is a meshless method that incorporates features of both Smoothed Particle Hydrodynamics and the Finite Volume Method. Here, two new formulations are presented which enhance its performance in simulation of free surface flows. One is a method for determining the velocity of the free surface, making use of a partial Riemann problem to analyse the flow between the particle barycentre and the geometric free surface. The second is a well-balanced formulation for gravity forces that enables hydrostatic equilibrium to be preserved exactly. Results are presented for hydrostatic, 1D impact, dambreak and deep-water standing wave test cases. Computations display convergence and good agreement with experimental data. The new methods recover exact hydrostatic equilibrium, improve robustness and reduce acoustic pressure fluctuations in dambreak flows, and reduce dissipation.

1. Introduction

In this article, two modifications are proposed to the Finite Volume Particle Method (FVPM) to enhance advection of a dynamic free surface and to improve accuracy in hydrostatic simulations. FVPM, like Smoothed Particle Hydrodynamics (SPH), is a meshless method derived from a particle-based ker-

*Corresponding author.
Email address: nathan.quinlan@nuigalway.ie (Nathan J. Quinlan)

nel smoothing operation. In FVPM, the smoothing may be understood as a distribution of the volume assigned to each particle, with well-defined sharing of volume among overlapping neighbours. The method has strong similarities with mesh-based finite volume methods, and allows arbitrary choice of the particle transport velocity. It can be implemented in fully Lagrangian form, like SPH, making it a candidate for applications to flows with dynamic interfaces and free surfaces.

Jahanbakhsh *et al.* [1] analysed FVPM for free-surface flows and applied it to jet impingement, and later to flow in Pelton turbines [2]. However, to date, FVPM has not been validated or characterised in detail for benchmarks such as hydrostatic cases and dam-break flows. In the present article, two enhancements are proposed for simulation of free surfaces. The first is a novel method to determine the arbitrary Lagrangian Eulerian (ALE) transport velocity for particles on the free surface. Purely Lagrangian particle transport is a natural choice for a particle method in free-surface flow. However, the free surface is not located at the centre of free-surface particles, and thus an error may be introduced by assuming the free-surface velocity equal to the particle velocity. In FVPM this distinction is rigorous. In the proposed new method, a refined calculation of the velocity at each particle's free surface is used as the ALE particle transport velocity. The method is explained in detail in section 3.1.

The second innovation concerns the discretisation of weight (or other body forces). The exact zero-order consistency of FVPM enables a well-balanced scheme in which weight and pressure gradient can be in exact equilibrium in a hydrostatic scenario. This method is presented in section 3.2.

Results of numerical tests are presented in section 4. Tests are selected to evaluate the effects of the new development and the performance of the method as a whole in free-surface flow, with comparisons against experimental and analytical benchmarks. The test cases are a hydrostatic tank, one-dimensional impact, the dambreak experiment of Lobovský *et al.* [3], and a standing wave.

2. The Finite Volume Particle Method

2.1. Principles

FVPM was introduced independently by Hietel *et al.* [4] and Ismagilov [5], and further analysed by Keck and Hietel [6] and Junk [7]. Here, the derivation is briefly outlined. FVPM is applied to a conservation equation of the form

$$\frac{\partial \mathbf{U}}{\partial t} + \nabla \cdot \mathbf{F}(\mathbf{U}) = 0 \ , \tag{1}$$

where $\mathbf{U}$ is the vector of conserved variables and $\mathbf{F}$ is the flux. The continuum is discretised by a set of particles, each one associated with a test function

$$\psi_i(\mathbf{x}, t) = \frac{W_i(\mathbf{x(t)})}{\sum_j W_j(\mathbf{x(t)})} \ . \tag{2}$$

The compactly supported kernel-like particle weight function $W_i(\mathbf{x}, t)$ is zero outside Ω_i, the support of particle i. Where a point is covered by multiple overlapping particles, $\psi_i(\mathbf{x}, t)$ can be interpreted as the fraction of a local volume element assigned to particle i, since $\sum_i \psi_i(\mathbf{x}, t) = 1$. Therefore the total volume of particle i is defined as

$$V_i = \int \psi_i(\mathbf{x}, t) \mathrm{d}\mathbf{x} \ . \tag{3}$$

Multiplying (1) by $\psi_i(\mathbf{x}, t)$ and integrating, after some manipulation, the following semi-discrete equation results:

$$\frac{\mathrm{d}}{\mathrm{d}t} \int_\Omega \psi_i(\mathbf{x}, t) \mathbf{U} \mathrm{d}\mathbf{x} + \sum_j \boldsymbol{\beta}_{ij} \cdot \boldsymbol{\mathcal{G}}_{ij} + \boldsymbol{\beta}_i^b \cdot \boldsymbol{\mathcal{G}}_i^b = 0 \ . \tag{4}$$

Here, $\dot{\mathbf{x}}_i$ is the transport velocity of particle i, which may be chosen arbitrarily. The numerical flux function $\boldsymbol{\mathcal{G}}_{ij} = \boldsymbol{\mathcal{G}}(\tilde{\mathbf{U}}_{ij}, \tilde{\mathbf{U}}_{ji}, \dot{\mathbf{x}}_i, \dot{\mathbf{x}}_j)$ approximates $\mathbf{F}(\mathbf{U}(\mathbf{x}_{ij}))$, as in the classical finite volume method (FVM), and also accounts for transport between particles i and j due to relative motion. The interface states $\tilde{\mathbf{U}}_{ij}$ and $\tilde{\mathbf{U}}_{ji}$ are reconstructed from the barycentres $\mathbf{b}_i$ and $\mathbf{b}_j$ respectively, with the linear reconstruction $\tilde{\mathbf{U}}_{ij} = \mathbf{U}_i + \tilde{\nabla}\mathbf{U}_i \cdot (\mathbf{x}_{ij} - \mathbf{b}_i)$, (where $\tilde{\nabla}$ denotes a meshless approximation to the gradient) or zero-order reconstruction $\tilde{\mathbf{U}}_{ij} = \mathbf{U}_i$.

The quantity $\boldsymbol{\beta}_{ij}$ denotes $\boldsymbol{\gamma}_{ij} - \boldsymbol{\gamma}_{ji}$, where

$$\boldsymbol{\gamma}_{ij} = \int_\Omega \frac{W_i(\mathbf{x}) \nabla W_j(\mathbf{x})}{\left(\sum_k W_k(\mathbf{x})\right)^2} \mathrm{d}\mathbf{x} \ . \tag{5}$$

Boundary terms are denoted by the superscript b and

$$\boldsymbol{\beta}_i^b = \int_{\partial\Omega} \psi_i(\mathbf{x}, t) \mathrm{d}\mathbf{S} \,, \tag{6}$$

where $\mathbf{S}$ is outward-normal boundary area. The derivation of Eq. (4) is presented in detail by Hietel *et al.* [4].

Equation (4) is similar in structure to the mesh-based FVM, with $\boldsymbol{\beta}_{ij}$ and $\boldsymbol{\beta}_i^b$ taking the place of cell-cell and cell-boundary interface areas. Accordingly, $\boldsymbol{\beta}_{ij}$ is known as the interparticle area. Definition (5) implies $\sum_j \boldsymbol{\beta}_{ij} = 0$, which ensures zero-order consistency, and $\boldsymbol{\beta}_{ij} = -\boldsymbol{\beta}_{ji}$, which ensures conservation. Cell face areas in FVM satisfy the same conditions.

The rate of change of particle volume is given by differentiation of Eq. (3) as

$$\frac{d}{dt} V_i = \sum_j \left[\boldsymbol{\gamma}_{ij} \cdot \dot{\mathbf{x}}_j - \boldsymbol{\gamma}_{ji} \cdot \dot{\mathbf{x}}_i \right] . \tag{7}$$

The method also defines the centroid of particle volume, or barycentre,

$$\mathbf{b}_i = \int \psi_i(\mathbf{x}, t) \mathbf{x} \mathrm{d}\mathbf{x} \,. \tag{8}$$

The barycentre is not generally equal to the particle centre $\mathbf{x}_i$, which is used to construct the weight function W_i. Typically, particle supports are circular, spherical, square or cubic, and $\mathbf{x}_i$ is simply the geometric centre of the support. The quantity $\int_\Omega \psi_i(\mathbf{x}, t) \mathbf{U} \mathrm{d}\mathbf{x}$ in Eq. (4) is the volume-weighted average of $\mathbf{U}$ over the particle, and is labelled $\mathbf{U}_i$. Hietel *et al.* [4] showed that $\mathbf{U}_i$ is a second-order approximation to the value of $\mathbf{U}$ at the barycentre $\mathbf{b}_i$.

Most FVPM implementations use a Godunov-type method to determine the interparticle flux $\boldsymbol{\mathcal{G}}(\mathbf{U}_i, \mathbf{U}_j)$. In the basic version, the flux is derived from the solution of a Riemann problem with initial states $\mathbf{U}_i$ and $\mathbf{U}_j$, i.e. zero-order reconstruction from barycentres to particle interfaces. Nestor *et al.* [8] introduced a higher-order scheme based on the MUSCL finite volume approach [9]. Gradients of field variables at particle barycentres are estimated using a meshless numerical operator, and a non-linear limiter is applied. The limited gradients are used to estimate field values at particle interfaces to second-order

accuracy. These reconstructed values are the initial states used to determine interparticle fluxes using a Riemann solver. In principle, the reconstruction operation can be performed using any meshless approximation of the required accuracy (specific details of the present implementation are given in section 2.5 below).

The FVPM defined and named by Hietel *et al.* [4] is unrelated to several similarly named methods [10, 11, 12]. FVPM in the present work is characterised uniquely by its definitions of interparticle area (5) and particle volume (3), which are rigorously derived from the weak form of the conservation PDE.

2.2. Evaluation of interparticle area

In the first versions of FVPM, $\boldsymbol{\beta}_{ij}$ was calculated by Gaussian quadrature, which is extremely expensive and an additional source of error. Quinlan *et al.* [13, 14] defined $W_i(\mathbf{x})$ as the top-hat function, equal to 1 inside the support of particle i and 0 elsewhere. The integral of Eq. (5) can be computed analytically, quickly and exactly. This approach was extended to 3D by Jahanbakhsh *et al.* for cubic [1] and spherical [2] particles. Another approach for exact calculation of $\boldsymbol{\beta}_{ij}$, using splines for $W_i(\mathbf{x})$ in 1D, was proposed by Kaland [15].

2.3. Consistency and convergence

A minimum of zero-order consistency is ensured, since $\sum_j \boldsymbol{\beta}_{ij} = 0$. With a uniform value for flux $\mathcal{G}_{ij}$ in Eq. (4), the time derivative evaluates to zero, and thus a uniform field is preserved. The method is modelled on the second-order finite volume first-order Godunov and second-order MUSCL schemes, with constant or linear reconstruction respectively. However, as yet there is no complete theoretical analysis of the order of consistency or convergence of FVPM. The approximation steps that influence spatial accuracy are the FVPM gradient operator $\nabla \cdot \mathbf{F} \approx \sum_j \boldsymbol{\beta}_{ij} \mathbf{F}_{ij}$ [6], the Godunov-type calculation of fluxes, the selection of the interface points $\mathbf{x}_{ij}$ [6], and weighted volume-averaging (proven second-order accurate [6]). Further work is required to analyse these effects in detail.

In the present work, the main variant used is the linear reconstruction from barycentre to interface, similar to the second-order MUSCL finite volume scheme. Numerical tests of FVPM with linear reconstruction have previously displayed second-order convergence in Poiseuille flow [8] and Taylor-Green flow [8, 16, 14]. The zero-order reconstruction is used in some cases for comparison.

2.4. Free surfaces in FVPM

In FVPM, the free surface is defined as all regions of all particle support boundaries $\partial\Omega_i$ that are not covered by any other particle, as shown in Fig. 1. This gives an unambiguous definition of the mechanical free surface as a geometric surface in 3D (curve in 2D).

To facilitate the following discussion, a virtual void particle v is defined for each fluid particle i, as shown in Fig. 1. (This particle does not appear in the method in practice.) It overlaps only with one fluid particle i, with infinitesimal volume of overlap. The free-surface region of $\partial\Omega_i$ (the region $\partial\Omega_i$ not covered by any other fluid particle) is fully covered by v. To maintain these conditions, v must be advected at the same velocity as i, i.e. $\dot{\mathbf{x}}_v = \dot{\mathbf{x}}_i$.

2.4.1. Mass and momentum

At the interface between i and v, the free-surface dynamic boundary condition must be enforced. There should be zero flux of momentum between the void and the fluid. Similarly there should be no mass flux. Since FVPM is formulated in terms of fluxes, it is straightforward to implement this. The void simply makes no contribution to the sum of fluxes in Eq. (4). There is no need to enforce $p = 0$ at the surface particles. To do so would result in a first-order error, since $p = 0$ should apply at the particle's free surface, but field values are defined only at the barycentre.

2.4.2. Volume

Although there is no exchange of mass and momentum bewteen the fluid and the void, Jahanbakhsh *et al.*[1] have noted that there is a conservative exchange of volume. If particle i advances into the void, for example, it gains the volume

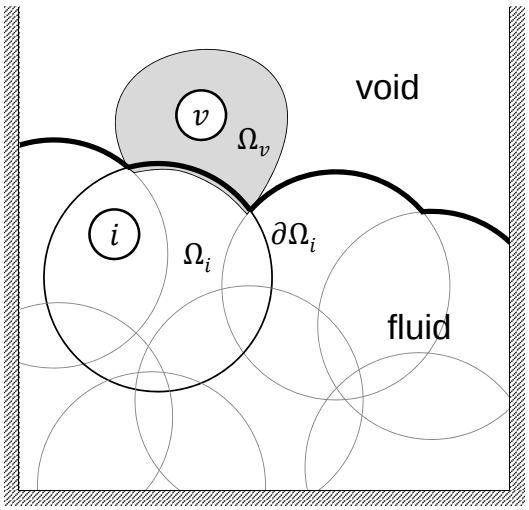

Figure 1: Schematic diagram of a particle i on the free surface with an implicit void particle v.

swept out by the exposed segment of $\partial\Omega_i$ (while also exchanging volume with its neighbour particles, depending on their relative motion). The transfer of volume from v to i is given by Eq. (7), making use of $\dot{\mathbf{x}}_v = \dot{\mathbf{x}}_i$ as follows.

$$\frac{\mathrm{d}V_{i,v}}{\mathrm{d}t} = [\boldsymbol{\gamma}_{iv} \cdot \dot{\mathbf{x}}_v - \boldsymbol{\gamma}_{vi} \cdot \dot{\mathbf{x}}_i] = \boldsymbol{\beta}_{iv} \cdot \dot{\mathbf{x}}_i \tag{9}$$

Since $\sum_j \boldsymbol{\beta}_{ij} = 0$, it follows that $\boldsymbol{\beta}_{iv} = -\sum_{j \neq v} \boldsymbol{\beta}_{ij}$. Therefore, Eq. 9 can simply be written as

$$\frac{\mathrm{d}V_i}{\mathrm{d}t} = \sum_j \left[\boldsymbol{\gamma}_{ij} \cdot \dot{\mathbf{x}}_j - \boldsymbol{\gamma}_{ji} \cdot \dot{\mathbf{x}}_i\right] - \sum_j \boldsymbol{\beta}_{ij} \cdot \dot{\mathbf{x}}_i \ , \tag{10}$$

where the particle v is discarded and summations are understood to be over all fluid neighbour particles. The void particles were introduced only for the sake of this argument, and need never be implemented in practice. $\sum_j \boldsymbol{\beta}_{ij}$ is interpreted as the free surface of particle i (normal from the void into the particle), just as $\boldsymbol{\beta}_{ij}$ is interparticle area.

2.4.3. Interparticle area

The above approach depends on enforcement of the consistency condition $\sum_j \boldsymbol{\beta}_{ij} = 0$. In early FVPM work, $\boldsymbol{\beta}_{ij}$ was approximated by quadrature of Eq. (5). Later its accuracy was improved by corrections that enforce that condition [17, 18]. These corrections were found necessary to achieve an acceptable balance between overall accuracy and computation time in flows without free surfaces. At the free surface, however, $\sum_j \boldsymbol{\beta}_{ij} = 0$ does not hold, and should not be enforced artificially. Thus, approximate $\boldsymbol{\beta}_{ij}$, based on quadrature, cannot be corrected at the free surface using available methods.

Consequently, exact evaluation of $\boldsymbol{\beta}_{ij}$ [14] is an essential enabling technique for free-surface modelling. It ensures $\sum_j \boldsymbol{\beta}_{ij} = 0$ is satisfied exactly in the interior of the fluid, wherever there are no gaps between particle supports. At the free surface, the non-zero $\sum_j \boldsymbol{\beta}_{ij}$ represents the surface area of a particle which is exposed to the void.

2.5. Numerical details

In the present work, the top-hat particle weight function is used to allow exact calculation of $\boldsymbol{\beta}_{ij}$ [14]. Gradients are calculated using SPH operators with the B-spline kernel, with the correction of Bonet and Lok [19] for first-order consistency. The Barth-Jespersen slope limiter [20] for unstructured meshes is applied and Liou's AUSM$^+$-up approximate Riemann solver [21] is used. Time-stepping is by the second-order Runge-Kutta scheme. Fluid is modelled as weakly compressible, using the modified Tait equation of state with $\gamma = 7$. Particle motion is purely Lagrangian throughout the numerical tests presented in this work, i.e. $\dot{\mathbf{x}} = \mathbf{u}$, unless otherwise stated. Although ALE particle velocity correction (shifting) has been employed successfully in FVPM [8, 1], in the present work it is not used, to allow other effects to be observed more clearly.

3. New extensions of FVPM for free-surface flow

3.1. Enhanced free-surface particle transport velocity

As discussed in section 2.4, if the free surface in FVPM is modelled without any special treatment, the mass and momentum fluxes between the particle and the void are zero. This enforces the correct dynamic boundary condition at the free surface. The material velocity $\mathbf{u}$ of free-surface particles is updated through the conservation equations. FVPM is an ALE method, and particle transport velocity $\dot{\mathbf{x}}_i$ can be chosen arbitrarily. A natural choice for free-surface flows is Lagrangian particle motion, i.e. $\dot{\mathbf{x}}_i = \mathbf{u}_i$.

However, $\mathbf{u}_i$ of a free-surface particle is not strictly equal to the velocity of the free surface. The particle's nominal material velocity $\mathbf{u}_i$ is a weighted average of material velocity over the whole of particle i, and a second-order approximation to the value at the barycentre [4]. The free surface has a clear geometric definition, consisting of the exposed parts of particles' support boundaries, as shown in Fig. 2. The velocity of the free surface is the transport velocity $\dot{\mathbf{x}}$, which is arbitrarily chosen. The barycentre is separated from the free surface by a distance approximately equal to the particle radius, $2h$. Thus, in pure Lagrangian mode, when $\dot{\mathbf{x}} = \mathbf{u}$, there is a first-order error in the velocity of the free surface.

The purpose of the present work is to calculate a better approximation to the free-surface velocity, which can be applied as transport velocity $\dot{\mathbf{x}}$ for free-surface particles. This is entirely distinct from enforcement of the dynamic boundary condition, which imposes no conditions directly on velocity. A secondary aim is to improve robustness, since in fully Lagrangian mode, the present FVPM method sometimes fails in simulations of violent flows in regions of rapid free-surface deformation, such as breaking waves.

The approach is to solve a partial Riemann problem for the flow normal to the free surface at sub-particle scale, relating the known velocity and pressure at the barycentre to the known pressure ($p = 0$) and unknown velocity at the free surface. This is based on the method of Dubois [22], as adapted by Marongiu

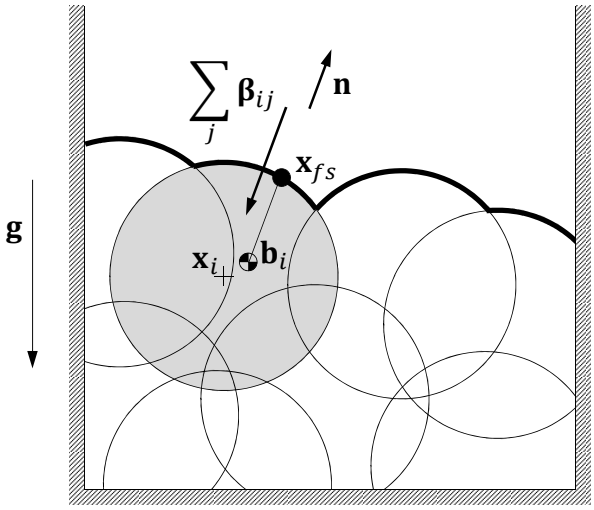

Figure 2: Schematic diagram of circular particles bounded by walls and a free surface. The free surface is marked with a heavy curve, $\mathbf{x}_i$ is the geometric centre of particle i (shaded), $\mathbf{b}_i$ is its barycentre, $\mathbf{g}$ is acceleration due to gravity, $\sum_j \boldsymbol{\beta}_{ij}$ is the projected area of the free-surface region of the surface of particle i, and $\mathbf{x}_{fs}$ is the projection of the barycentre onto the free surface.

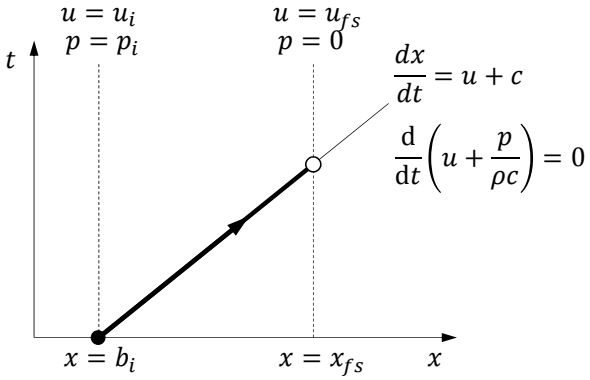

Figure 3: Space-time diagram of a characteristic wave in one dimension, propagating from the barycentre of particle i at $x = b_i$ to the free surface at $x = x_{fs}$.

et al. [23] for walls in SPH, and already employed for wall boundary conditions in the present FVPM method. The principle is illustrated in 1D in Fig. 3. The Riemann invariant $u + p/(\rho c)$ is constant along the wave running at velocity $u + c$ from the barycentre of particle i to the free surface, leading to

$$\left(u + \frac{p}{\rho c}\right)_i = \left(u + \frac{p}{\rho c}\right)_{fs} . \tag{11}$$

(For clarity, gravity is omitted from this discussion.) Since $p = 0$ holds at the free surface, Eq. (11) can be solved for the free-surface velocity

$$u_{fs} = u_i + \frac{p_i}{\rho_i c_i} . \tag{12}$$

Finally, $\dot{\mathbf{x}}_i$ is set to u_{fs}, so that the particle is transported at the correct velocity for the free surface.

In the multidimensional case, a 1D problem is solved for flow normal to the free surface. The geometry is shown in Fig. 2. The sum of the interparticle areas, $\sum_j \boldsymbol{\beta}_{ij}$, is the projected area of the particle's free surface, directed inwards normal to the surface. This is used to define the outward unit normal, $\mathbf{n}$. A representative point on the free surface, $\mathbf{x}_{fs}$, is located by projecting $\mathbf{b}_i$ onto the surface of the particle in the direction of $\mathbf{n}$. This is required to correct the Riemann invariant for hydrostatic pressure. The 1D Riemann problem is then

solved for the normal velocity, giving

$$\mathbf{u}_{fs} \cdot \mathbf{n} = \mathbf{u}_i \cdot \mathbf{n} + \frac{p_i + \rho_i \mathbf{g} \cdot (\mathbf{x} - \mathbf{x}_{fs})}{\rho_i c_i} \, . \tag{13}$$

This provides the surface-normal component of free-surface particle transport velocity, while the tangential component is set to the tangential component of the particle material velocity. The final form of the particle transport velocity is then

$$\dot{\mathbf{x}}_i = (\mathbf{u}_{fs} \cdot \mathbf{n})\, \mathbf{n} + \mathbf{u}_i - (\mathbf{u}_i \cdot \mathbf{n})\, \mathbf{n} \, . \tag{14}$$

This procedure requires identification of free-surface particles. In FVPM, this is unambiguous and comes at no extra cost. Since $\sum_j \boldsymbol{\beta}_{ij} = 0$ for interior particles, free-surface particles are simply those with non-zero sum of interparticle areas (allowing a tolerance for rounding errors).

It should be noted that this formulation is distinct from the enforcement of the free-surface boundary condition. As discussed in section 2.4.1, the flux across the free surface is zero, independently of the velocity of the free-surface particles.

3.2. Hydrostatic balance

For accurate computation of hydrostatic equilibrium, or flows where hydrostatic forces overwhelm dynamics, the gravity force must be treated with care. The sum of pressure and weight force on a particle can be computed in an obvious way as

$$\int_{\Omega_i} \nabla p \mathrm{d}\mathbf{x} - \rho \mathbf{g} V_i \, . \tag{15}$$

In the context of mesh-based methods, Botta *et al.* [24] stated the principle that for a hydrostatically well-balanced scheme, weight and pressure gradient should be discretised in the same manner so that their numerical errors cancel exactly. The expression above does not satisfy this rule, and in practice, large errors have been observed in numerical tests.

Instead, in the extended method, the force per unit volume is now written as $\nabla(p - \rho \mathbf{g} \cdot \mathbf{x})$. This leads to the FVPM discretisation of force on particle i

as

$$\mathbf{F}_i = \sum_j (p^*_{ij} - \rho_i \mathbf{g} \cdot \mathbf{x}_{ij}) \cdot \boldsymbol{\beta}_{\mathbf{ij}} \tag{16}$$

where p^*_{ij} is the interface pressure between particles i and j determined by a Riemann solver, and $\mathbf{x}_{ij}$ is the i-j particle interface location. Local variation in density is neglected.

In an exact hydrostatic pressure field, Eq. (16) evaluates as follows. The pressure $p(\mathbf{x})$ is given by $\rho\mathbf{g}\cdot\mathbf{x}$. The present FVPM implementation uses a first-order consistent SPH scheme to estimate gradients at the particle barycentre for use in a MUSCL-type scheme. The pressure and velocity gradients in this linear field are therefore recovered exactly as $\rho\mathbf{g}$ and zero, respectively, and the pressure and (zero) velocity are reconstructed exactly at the interface point $\mathbf{x}_{ij}$, from both the i and j sides. The Riemann problem at each interface, with identical left and right states, also returns the exact pressure, $p^*_{ij} = p_i + \rho_i \mathbf{g} \cdot (\mathbf{x}_{ij} - \mathbf{b}_i)$. Substituting this into (16), the force reduces to

$$\begin{aligned} \mathbf{F}_i &= \sum_j [p_i + \rho_i \mathbf{g} \cdot (\mathbf{x}_{ij} - \mathbf{b}_i) - \rho_i \mathbf{g} \cdot \mathbf{x}_{ij}] \cdot \boldsymbol{\beta}_{\mathbf{ij}} \\ &= [p_i - \rho_i \mathbf{g} \cdot \mathbf{b}_i] \cdot \sum_j \boldsymbol{\beta}_{\mathbf{ij}} \\ &= 0 \,, \end{aligned}$$

since $\sum_j \boldsymbol{\beta}_{\mathbf{ij}} = 0$. Thus, equilibrium is exact in a hydrostatic pressure distribution with uniform density.

For a particle at the free surface, Eq. (16) is applied, using $\mathbf{x}_{fs}$ (as defined in section 3.1 and Fig. 2) as the interface point $\mathbf{x}_{ij}$, and $-\sum_j \boldsymbol{\beta}_{ij}$ as the effective area. The pressure p^*_{ij} is zero.

For clarity, the above development omits limiters. Following standard practice in mesh-based finite volume methods, slope limiters are employed in FVPM to prevent the creation of new extrema in the reconstruction process. In the present work, the Barth-Jespersen slope limiter [20] is used. The limiter function

for particle i and a neighbour j is

$$\varphi_{ij} = \begin{cases} \min\left(1, \dfrac{\phi_i^{max} - \phi_i}{\nabla\phi_i \cdot (\mathbf{x}_{ij} - \mathbf{b}_i)}\right), & \text{if } \nabla\phi_i \cdot (\mathbf{x}_{ij} - \mathbf{b}_i) > 0 \\ \min\left(1, \dfrac{\phi_i^{min} - \phi_i}{\nabla\phi_i \cdot (\mathbf{x}_{ij} - \mathbf{b}_i)}\right), & \text{if } \nabla\phi_i \cdot (\mathbf{x}_{ij} - \mathbf{b}_i) < 0 \\ 1, & \text{if } \nabla\phi_i \cdot (\mathbf{x}_{ij} - \mathbf{b}_i) = 0 \end{cases}, \tag{17}$$

where ϕ denotes pressure or a velocity component and $\mathbf{x}_{ij} = \frac{1}{2}(\mathbf{x}_i + \mathbf{x}_j)$ is the interface point. Minima and maxima are taken over all neighbours of i. The limiter for particle i, φ_i, is then taken as the minimum of all pairwise limiters φ_{ij} and is applied to the gradient of ϕ in the reconstruction from barycentre to interface points:

$$\phi_{ij} = \phi_i + \varphi_i \nabla\phi_i \cdot (\mathbf{x}_{ij} - \mathbf{b}_i)\,, \tag{18}$$

where $\nabla\phi_i$ is determined by a first-order consistent SPH gradient operator in this case.

Limiter functions are non-linear, and when activated, they compromise the first-order consistency required for equilibrium. To avoid this, reconstruction and limiting operations are applied to the deviation from local hydrostatic pressure distribution, $\hat{p}^i(\mathbf{x}) = (p(\mathbf{x}) - p_i) - \rho_i \mathbf{g} \cdot (\mathbf{x} - \mathbf{x}_i)$, rather than to pressure $p(\mathbf{x})$ directly. The limiter is calculated for this variable according to Eq.(17). It is then reconstructed to $\mathbf{x}_{ij}$ by

$$\hat{p}^i_{ij} = \hat{p}^i_i + \varphi_i \tilde{\nabla}\hat{p}^i_i \cdot (\mathbf{x}_{ij} - \mathbf{b}_i) \tag{19}$$

and the result is converted back to absolute pressure

$$p_{ij} = p_i + \rho_i \mathbf{g} \cdot (\mathbf{x} - \mathbf{x}_i) + \hat{p}^i_{ij}\ . \tag{20}$$

This is used as input to the Riemann problem at the ij interface.

4. Numerical tests

4.1. Hydrostatics

4.1.1. Test case

Two geometries were used to test the hydrostatic balance model. One is a simple rectangular tank of width $2H$, filled to depth H. The second, referred

to as the irregular tank, has oblique surfaces. In both cases, particles are distributed with $\Delta x/H = 1/10$ and $h/\Delta x = 0.501$, and initialised with zero velocity and a hydrostatic pressure distribution. In a third test, the fluid in irregular tank is discretised with non-unifrom particles, ranging from $\Delta x/H = 1/10$ in most of the tank to a small region of $\Delta x/H = 1/40$ at the free surface, with $h/\Delta x = 0.501$ throughout. All results presented here were computed with the new hydrostatic balance formulation. Based on the reference velocity $(gH)^{1/2}$, the Reynolds number is 1.1×10^6 and Mach number is 0.04.

4.1.2. Results

Results are shown in Fig. 4 for the evolution of the total kinetic energy of the system. In the simple rectangular tank, kinetic energy, normalised with respect to the total gravitational potential energy, decays rapidly from 10^{-13} to 10^{-18}, on the order of machine zero. Energy is slightly higher in the irregular tank. Addition of the enhanced free-surface boundary condition has a minimal effect on the global energy. With particles of non-uniform size near the free surface, there is higher initial kinetic energy and slower decay. This is because the barycentre is not symmetrically located in particles with neighbours of different size, and some reconfiguration is necessary to reach exact equilibrium. Nonetheless, spurious velocity is at a negligible level, with dimensionless kinetic energy falling below 10^{-13} by $t^* \approx 50$.

Velocity fields are shown in Fig. 5 at the instant of maximum velocity for two cases. These indicate the maximum velocity that can be expected as the system approaches numerical equilibrium, on the order of $(10^{-4})\sqrt{gH}$ with non-uniform particles.

To examine convergence, simulations were carried out for a simple tank with regularly distributed particles 5 to 100 deep. Computed steady-state pressure distributions are shown in Figure 6. Results display second-order convergence to the analytical solution (21).

$$p(y) = \frac{\rho_0 c_0^2}{\gamma} \left\{ \left[1 + \frac{(\gamma - 1)g}{c_0^2}(H - y) \right]^{\frac{\gamma}{\gamma - 1}} - 1 \right\} \tag{21}$$

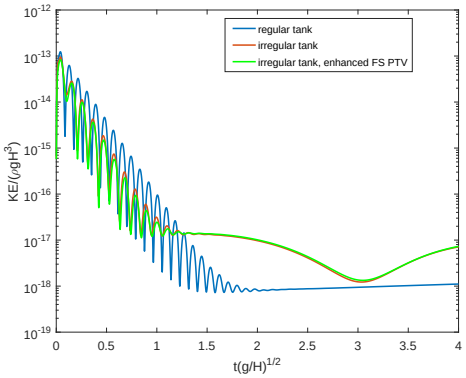

(a)

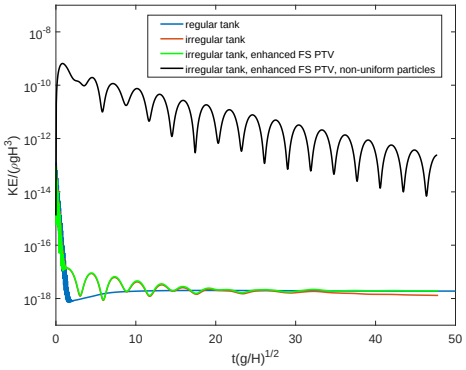

(b)

Figure 4: Dimensionless kinetic energy in the regular and irregular hydrostatic tanks, with the hydrostatic balance formulation, with and without enhanced free-surface particle transport velocity (FS-PTV). The same data is shown on different scales in the two plots.

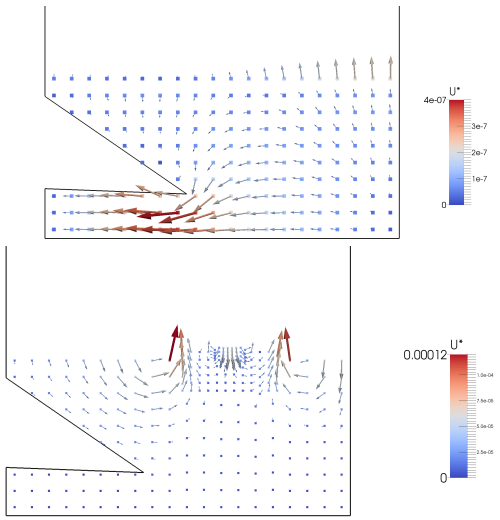

Figure 5: Non-dimensionalised velocity fields $U^* = |\mathbf{u}|/\sqrt{gH}$ in the irregular tank at the instant of maximum velocity in each case. (a) Lagrangian particle transport velocity and uniform particles, $t^* = 0.096$. (b) Enhanced free-surface particle transport velocity and non-uniform particles, $t^* = 0.596$. Note that particle positions are marked at their geometric centres, and support radius is proportional to spacing ($h/\Delta x = 0.501$). The tops of the free-surface particles are approximately aligned on a horizontal line, although the centres are not.

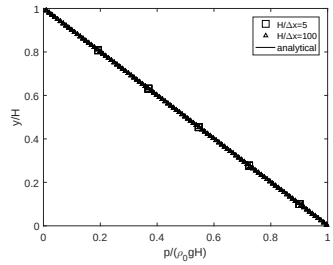

(a) Pressure distribution computed for two resolutions, with the analytical solution.

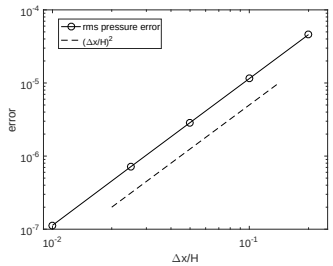

(b) Root mean square error in non-dimensionalised pressure.

Figure 6: Non-dimensionalised pressure $p/(\rho_0 gH)$ in a regular tank at $t^* = 10$, computed with the hydrostatic balance formulation.

4.2. Simple one-dimensional impact

4.2.1. Test case

In weakly compressible methods the sound speed is a numerical parameter, usually set below the physical value. Le Touzé *et al.* [25] and Marrone *et al.* [26] investigated the role of compressibility in SPH modelling of nearly incompressible fluids. Numerically and physically, transient impact pressure is dependent on the speed of sound. Waves resulting from impact may be dissipated by physical viscosity or numerical dissipation to yield a nearly incompressible flow at longer time scales.

A simple 1D impact flow has been simulated to evaluate compressibility and dissipation effects in FVPM, preliminary to simulations of an experimental dambreak flow in section 4.3. The problem is similar to the impact of two symmetric jets considered by Marrone *et al.* [26]. A fluid column of length L, at initial pressure 0, impacts on a wall at speed U and corresponding Mach number $M = U/c_0$. Theoretically, a shock wave is expected to propagate from the wall to the free surface, where it is reflected as a rarefaction. Alternating rarefaction and shock waves impact on the wall. For weak waves, which propagate at the reference speed of sound, the pressure ranges between 0 and $\rho U c_0$. Simulations were carried out with $L/\Delta x = 100$ and $h/\Delta x = 0.48$, for the FVPM variants with zero-order and linear reconstruction at $M = 0.001, 0.01, 0.1$, without the new free-surface or hydrostatic balance treatments (there is no gravity in this problem).

4.2.2. Results

With zero-order reconstruction (Fig. 7), waves rapidly become smeared to an approximately sinusoidal signal, and peak pressure decays by 50% by $t^* = tc_0/L \simeq 50$. With the linear reconstruction (MUSCL) scheme (Fig. 8), for $M = 0.01$ and $M = 0.001$, pressure remains essentially constant from cycle to cycle up to $t^* = 100$ and beyond, aside from a small under/overshoot which grows with time. At the highest Mach number, $M = 0.1$, non-linear compressibilty effects are significant, leading to more complex interactions and a decaying wave. At

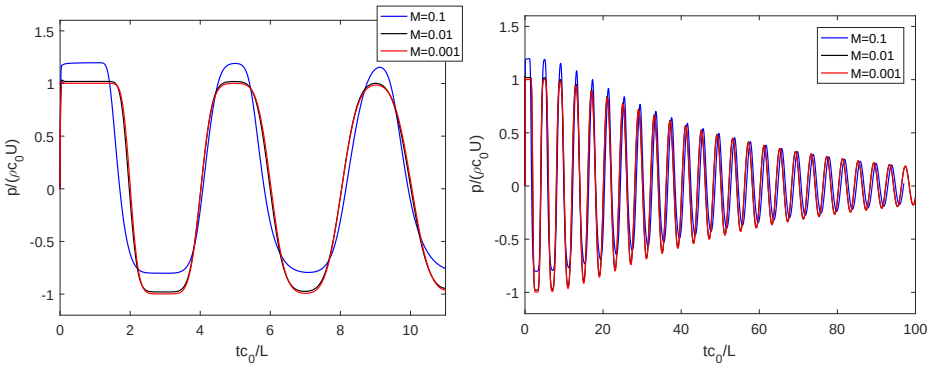

Figure 7: Wall pressure in the 1D impact test, computed using FVPM with zero-order reconstruction, shown on two time scales. Pressure is non-dimensionalised by theoretical acoustic impact pressure $\rho c_0 U$ and time by the acoustic transit time L/c_0. The same data is shown on different scales in both plots. (Computed without the new formulations.)

the lowest Mach numbers, normalised pressure $p/(\rho U c_0)$ is independent of Mach number when plotted as a function of normalised time tc_0/L. This confirms that the absolute magnitude and frequency of impact pressure scale with the speed of sound or inversely with Mach number.

Although there is negative pressure in these tests, there is no tensile instability. FVPM can suffer a discrete analogue of SPH tensile instability, if negative pressure occurs where there is a gap between particle supports. In this case, however, the expansion is not large enough to open a void. Neighbour overlap is defined by $h/\Delta x_0 = 0.48$ in this case, giving 2 neighbours per particle in 1D.

When the fluid is brought to rest by the shock wave, kinetic energy is stored by compression work $\int_{\rho_0}^{\rho} p\rho^{-2}\mathrm{d}\rho$. Energy alternates between kinetic and compression forms, as illustrated in Fig. 9 for FVPM with linear reconstruction at $M = 0.01$. Total energy should remain constant in the absence of dissipation, which may occur in strong shock waves (in cases of high Mach number) or as a result of numerical dissipation. In Fig. 10 it is evident that the total energy is dissipated rapidly in the scheme with zero-order reconstruction, whereas the higher-order variant approximately conserves the sum of kinetic and com-

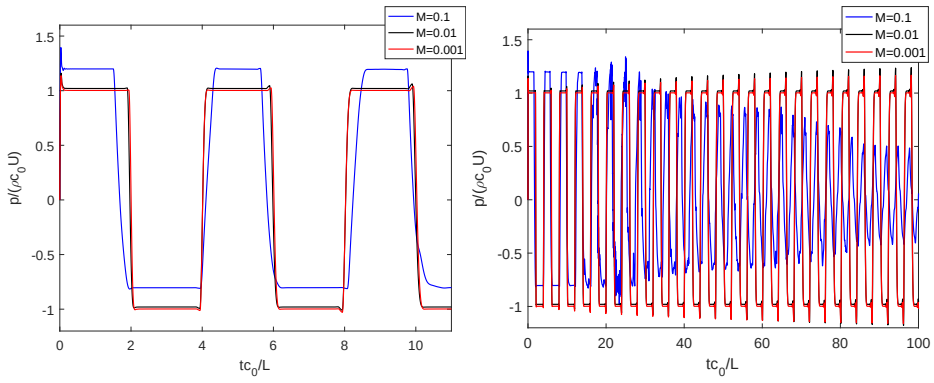

Figure 8: Wall pressure in the 1D impact test, computed using FVPM with linear reconstruction, shown on two time scales. Pressure is non-dimensionalised by theoretical acoustic impact pressure $\rho c_0 U$ and time by the acoustic transit time L/c_0. The same data is shown on different scales in both plots (computed without the new formulations).

pression energy for $M = 0.01, 0.001$, with losses less than 10% at $t^* \approx 96$ (24 cycles). For $M = 0.1$ there is much more rapid dissipation because of non-linear compressibility effects, as expected.

These benchmarks illustrate the effects of the choice of artificial sound speed, as discussed by previous researchers [25, 26]. They also highlight the contrast between the dissipative behaviour of FVPM with zero-order reconstruction and the very low dissipation in the higher order scheme.

4.3. Dambreak

4.3.1. Test case and experimental data

This simulation models the dambreak experiments of Lobovský *et al.* [3]. As shown in Fig. 11, a volume of still water of height H is initially retained behind a vertical gate, which is removed to initiate flow. The experiment was conducted 100 times. In the present work, the experimental case $H = 300$ mm was simulated with inviscid fluid and free-slip walls, and $h/\Delta x = 0.48$, giving 8 neighbours per particle in the initial configuration. In most simulations, the speed of sound is set for a reference Mach number $M = \sqrt{gH}/c_0 = 0.05$.

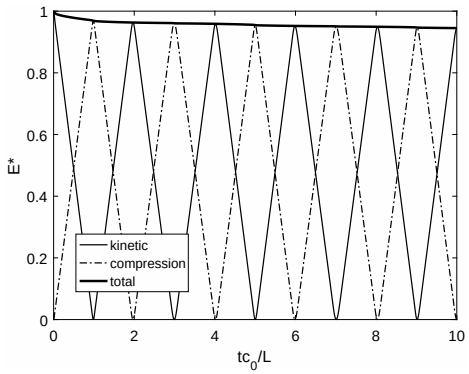

Figure 9: Total energy in the 1D impact test at M=0.01 in FVPM with linear reconstruction, non-dimensionalised with respect to initial kinetic energy (computed without the new formulations).

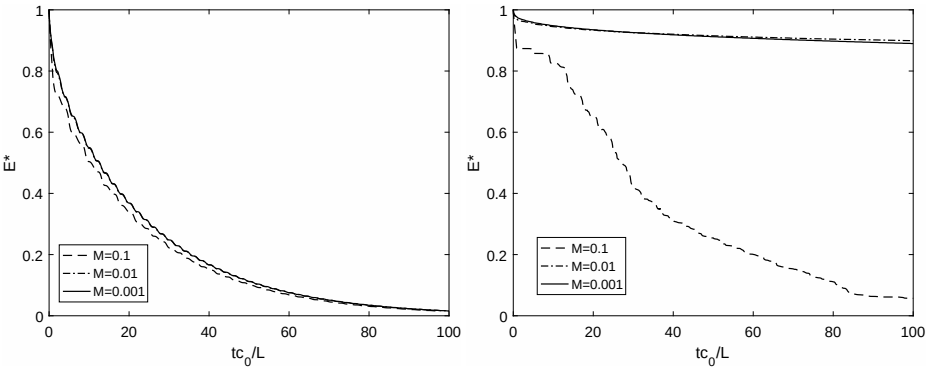

(a) First order (b) Second order

Figure 10: Sum of kinetic and compression energy in the 1D impact test, non-dimensionalised with respect to initial kinetic energy (computed without the new formulations).

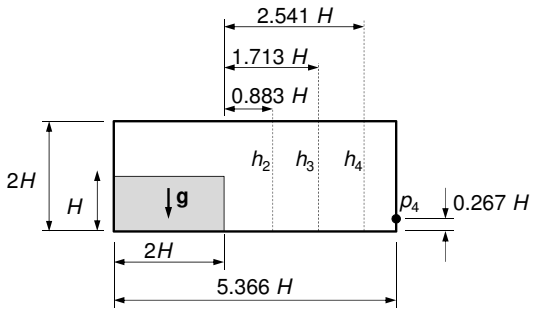

Figure 11: Schematic diagram of the model of the dambreak experiment of Lobovský *et al.*[3], showing the location of pressure sensor p_4 and water height measurements h_2, h_3 and h_4.

With velocity up to $2\sqrt{gH}$ occurring in the flow, the maximum Mach number occurring is approximately 0.1. The new hydrostatic balance formulation is used in all dambreak simulations presented. Without it, significant errors have been observed as the tank approaches equilibrium in the long term, but effects on the initial transient are negligible. Computational results are compared with experimental measurements of water height at three locations, and pressure at one location on the downstream wall.

A video recording of one experiment [27] was analysed to record gate position as a function of time with uncertainty estimated as ± 5 mm. The median over all 100 experiments of the gate removal mean velocity was reported as 3.46 m/s ($\approx 2\sqrt{gH}$). An analytical function was fitted to the video data, and scaled to 3.46 m/s, as shown in Fig. 12. This function was used to prescribe simulated gate motion.

4.3.2. Results

Sample pressure fields are shown in Fig. 13. Pressure distribution is smooth in space. Run-up on the downstream wall and the plunging secondary wave are captured.

The effect of the enhanced free-surface particle transport velocity formulation is illustrated by Fig. 14, showing wall pressure p_4. In comparison with a model based on a simple Lagrangian free surface, the new boundary condition

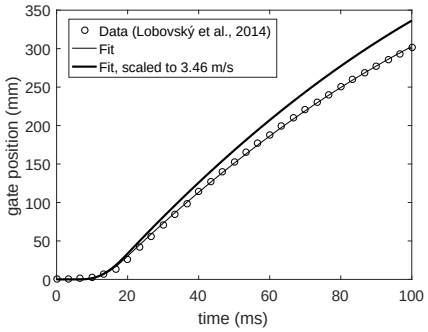

Figure 12: Data from one experiment of Lobovský *et al.*[3] for gate removal, with the fitted function, and the same function scaled to give the reported median gate velocity.

results in lower pressure oscillations. It also provides a more robust simulation. Without any additional treatment such as particle velocity correction (shifting), the simulation with a simple Lagrangian free surface fails at $t^* \approx 4.5$ due to locally poor particle distributions. The motivation for the new method is to provide correct motion for the free surface, rather than the geometric centre, of each particle.

Wall pressure p_4, computed with various resolutions, is compared quantitatively with experimental data [3] in Fig. 15. High-frequency oscillation is evident in the computational results at low resolution. The amplitude of this oscillation decreases rapidly as Δx is decreased and the pressure converges.

Numerical experiments have been conducted to investigate the relationship between high-frequency oscillations in the dambreak and the acoustic waves discussed in section 4.2 above. Results for various Mach number in Fig. 16 show that amplitude of oscillations increases as Mach number is decreased. Results of a computation with zero-order reconstruction are shown in Fig. 17. In comparison with Fig. 15, oscillations are greatly reduced by the increased dissipation in the lower-order scheme. Together, these results confirm that the oscillations observed in Fig. 15 are due to acoustic waves, which are preserved as a result of the inherent low dissipation of FVPM with linear reconstruction.

To suppress unwanted acoustic noise in weakly compressible SPH, Kiara *et*

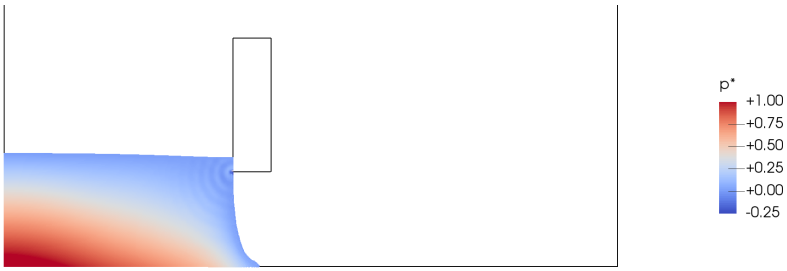

(a) $t^* = 0.43$, gate lifting.

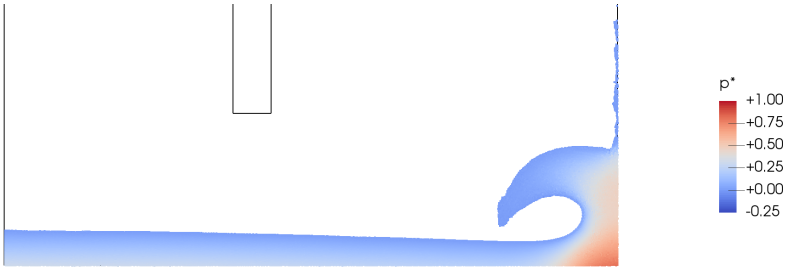

(b) $t^* = 6.15$, gate removed.

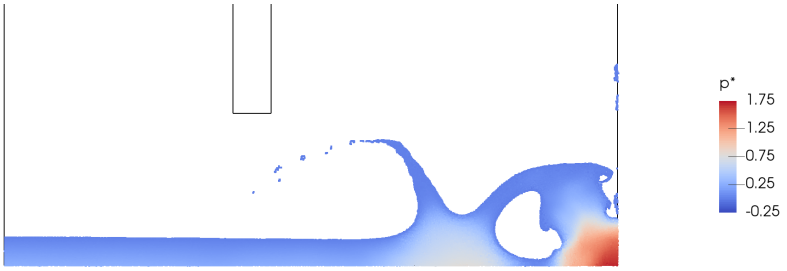

(c) $t^* = 7.15$, gate removed.

Figure 13: Dimensionless pressure $p^* = p/(\rho g H)$ in the dambreak flow with $H/\Delta x = 120$, $M = 0.05$, linear reconstruction, and new formulations for hydrostatic balance and enhanced free surface particle transport velocity. Note change of scale in (c).

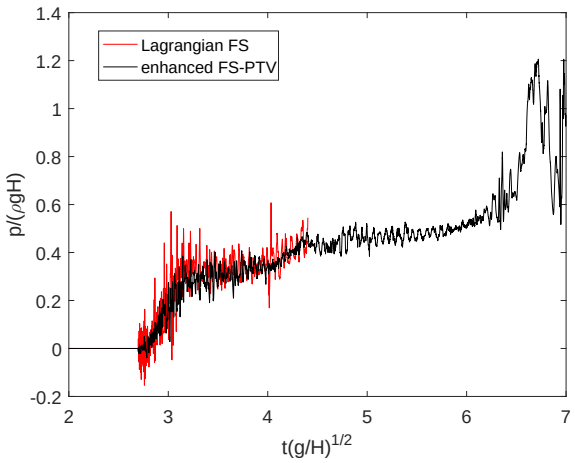

Figure 14: Computed pressure p_4 on the downstream wall for $H/\Delta x = 60$ and $M = 0.05$ and linear reconstruction, with and without the enhanced free surface particle transport velocity, with the new formulation for hydrostatic balance.

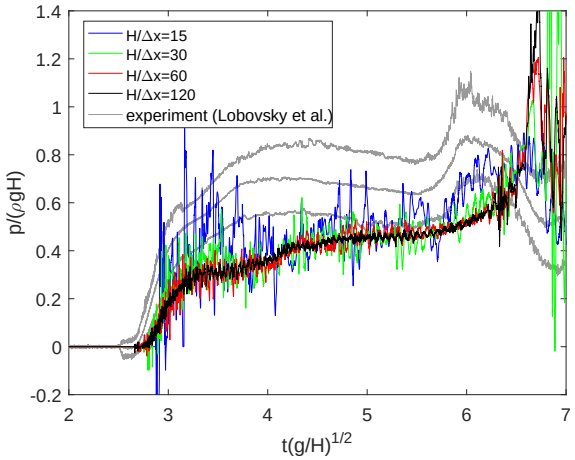

Figure 15: Computed pressure p_4 on the downstream wall for various $H/\Delta x$, with Mach number $M = \sqrt{gH}/c_0 = 0.05$, linear reconstruction, and enhanced free surface particle transport velocity. Also shown are the 2.5, 50 and 97.5 percentiles of the experimental data [3].

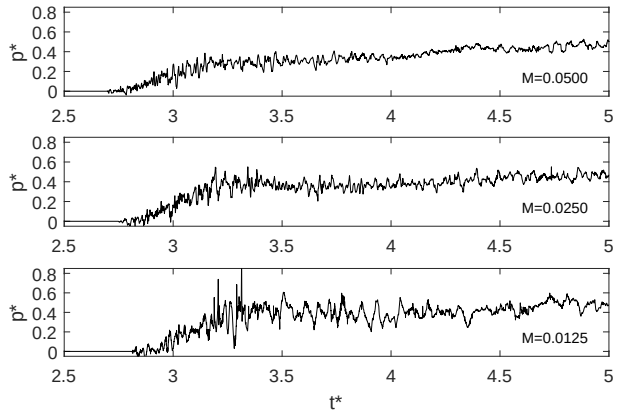

Figure 16: Computed pressure p_4 on the downstream wall for various Mach number $M = \sqrt{gH}/c_0$, with $H/\Delta x = 60$, linear reconstruction, and the new formulations for free surface particle transport velocity and hydrostatic balance.

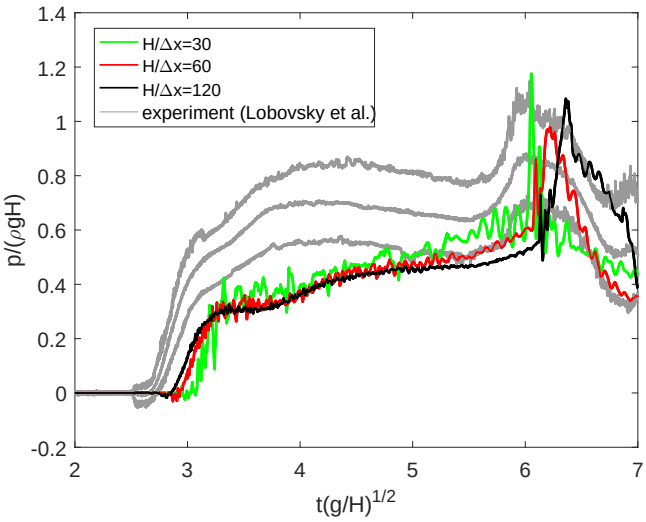

Figure 17: Computed pressure p_4 on the downstream wall for various $H/\Delta x$, with Mach number $M = \sqrt{gH}/c_0 = 0.05$, zero-order reconstruction, and the new formulations for free surface particle transport velocity and hydrostatic balance. Also shown are the 2.5, 50 and 97.5 percentiles of the experimental data [3].

al. [28] and Meringolo *et al.* [29] have proposed filtering approaches, based on the observation that the acoustic signal can often be distinguished from the underlying incompressible flow [25]. Here, a relatively crude post-processing approach is taken to smooth the FVPM pressure data of Fig. 15. The characteristic frequency for acoustic signals in the initial water column of height H is $c_0/(4H)$. A second-order low-pass Butterworth filter is applied with cut-off at half this frequency, i.e. $c_0/(8H)$. Filtered data in Fig. 18, along with the raw data in Fig. 15, allow easier examination of convergence and comparison with experiment.

Before plunging of the secondary wave at $t^* \approx 6.6$, the underlying low-frequency pressure signal is converged for all but the coarsest particles, $H/\Delta x \geq 30$. For the pressure peak at $t^* \approx 6.6$, there is good convergence at $H/\Delta x = 60$, and reasonable agreement on the magnitude of the peak with the higher end of the range of experimental pressure. In comparison with experiment, the pressure levels are generally lower. Similar reduced pressure was observed by other authors simulating the same experiment with single-phase SPH [30] and two-phase particle finite element method [31]. The peak pressure is delayed with respect to the experimental results; this has also been observed in other numerical simulations and has been shown to be due to the absence of the air phase [32, 30].

All dambreak results presented in Figs. 13 to 18 were obtained with the dynamic gate velocity function shown in Fig. 12 (scaled to 3.46 m/s mean velocity) prescribed for the removal of the gate. To investigate the sensitivity of results to the gate removal model, two other models for gate removal were investigated. The no-gate case represents instantaneous gate removal with an incompressible fluid. The instantaneous pressure field at $t = 0$ was determined by a finite-difference solution of the Laplace equation, with boundary conditions of zero pressure at the free surface and zero normal pressure gradient at the walls, following the approach of Stansby *et al.* [33]. The unsteady simulation then proceeded as usual with the weakly compressible model. In the third case, the gate was started impulsively and lifted at constant velocity of 3.46 m/s.

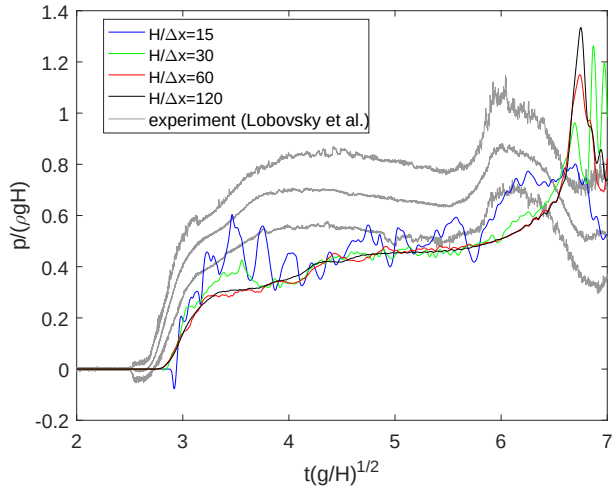

Figure 18: Computed pressure p_4 on the downstream wall for Mach number $M = \sqrt{gH}/c_0 = 0.05$, with $H/\Delta x = 60$, linear reconstruction, new formulations for free surface particle transport velocity and hydrostatic balance, and low-pass filter applied at $c_0/(8H)$ (14.2 Hz). See Fig. 15 for raw data. Also shown are the 2.5, 50 and 97.5 percentiles of the experimental data [3].

Results are shown in Fig. 19. In all three cases, as in the experiments, the pressure rise on the downstream wall occurs in two stages, both approximately linear in time, with a much higher rate in the first stage. With either a fully dynamic or constant-velocity gate, the first impact is later than without a gate, and pressure reaches a higher level in the initial rapid stage. This behaviour is closer to the experimental results. These moving-gate results suggest that modelling the finite gate removal time is necessary for accurate prediction of the early transient stages of flow far downstream, but the results are not sensitive to the detailed kinematics of the gate.

Results for water height are shown in Fig. 20, with experimental measurements from an arbitrarily selected run. Transient peaks in water height for the finer resolutions are due to particles splashing high above the bulk of liquid. Apparent noise at low resolution is because the free surface in FVPM consists of circular arc segments of the particles' support boundaries (see Fig. 2), and the numerical water height sensor detects the highest point of the particles cov-

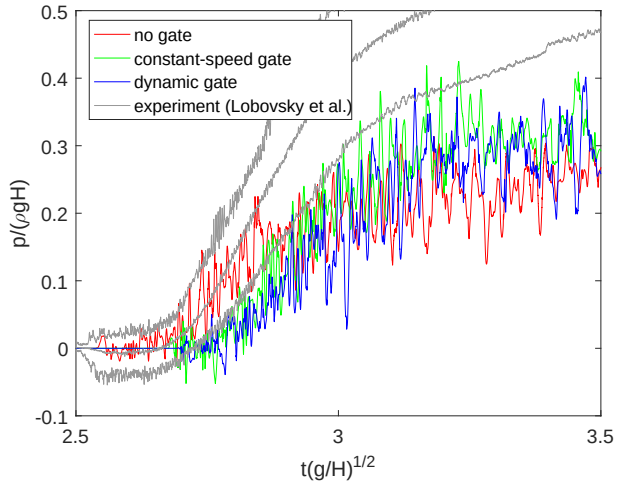

Figure 19: Computed pressure p_4 on the downstream wall for Mach number $M = \sqrt{gH}/c_0 = 0.05$, with $H/\Delta x = 60$, linear reconstruction, and the new formulations for free surface particle transport velocity and hydrostatic balance, for no gate (instantaneous gate removal), gate removal at constant speed of 3.46 m/s, and a dynamic gate as shown in Fig. 12. Also shown are the 2.5, 50 and 97.5 percentiles of the experimental data [3].

ering its x location. Before impact on the downstream wall, FVPM results agree closely with the experiment for all resolutions, even $H/\Delta x = 15$. After breaking of the secondary wave ($t^* \approx 6.6$) there is satisfactory convergence at h_4 (the transducer closest to the downstream wall). As the reflected waves propagate leftwards to h_3 and h_2, with more complex and violent dynamics observed in the experiments, results become increasingly sensitive to resolution.

4.4. Standing wave

4.4.1. Test case

Results are presented here for a standing wave in an inviscid fluid, following Antuono *et al.*[34]. A potential solution gives the velocity field as

$$\mathbf{u}(x, y, t) = -\nabla \left(\epsilon \frac{Hg}{2\omega} \frac{\cosh[k(y + H)]}{\cosh(kH)} \cos(kx) \cos(\omega t) \right) . \tag{22}$$

For an inviscid fluid, the wave should oscillate without loss of energy. The circular frequency ω is $[gk \tanh(kH)]^{1/2}$, H is depth, and $\epsilon = 2A/H$ where A is

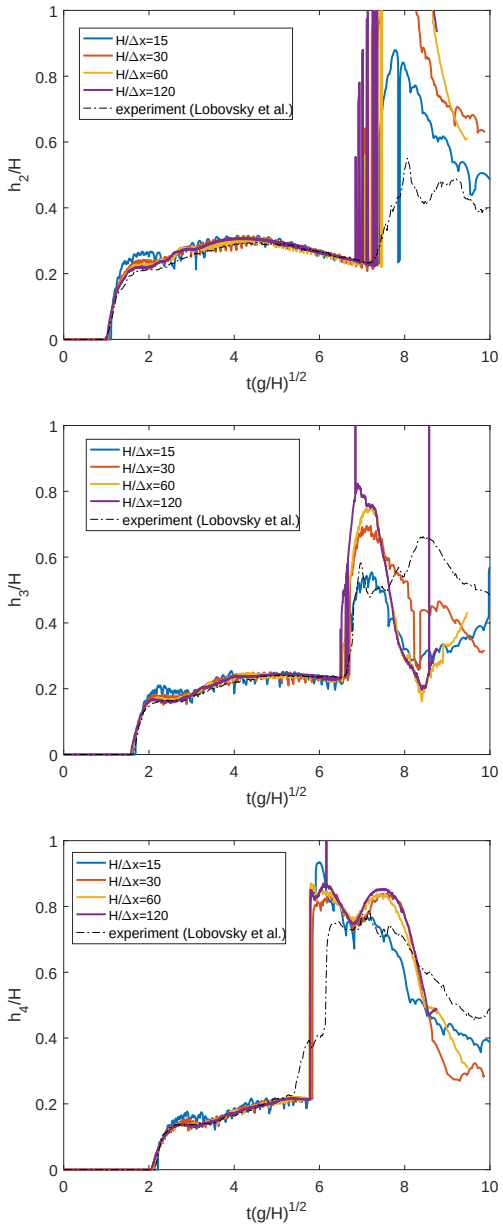

Figure 20: Computed water depth in the dambreak problem for various $H/\Delta x$, compuoted with the new formulations for free surface particle transport velocity and hydrostatic balance, along with data from a single experiment [3],

amplitude. The domain has periodic boundaries at $x = 0, H$ and a wall at $y = -H$. The fluid is initialised with a level free surface at $y = 0$ and the analytical velocity field (22) evaluated at $t = 0$, and hydrostatic pressure. The amplitude parameter ϵ is 0.05 and $H/\Delta x$ ranges from 20 to 160, with $h/\Delta x = 0.48$ in all cases. The new hydrostatic balance formulation is applied, and results are presented with and without the new free-surface particle transport formulation.

The test case is used here to assess the dissipative behaviour of the method. In the viscous case, the kinetic energy decays as

$$E_k(t) = \frac{\epsilon^2 g H^3}{32} \, \mathrm{e}^{-4\nu k^2 t} [1 + \cos(2\omega t)] \, , \tag{23}$$

where ν is kinematic viscosity [35]. By fitting numerical results to this function, an effective viscosity can be calculated. This in turn is used to determine an effective Reynolds number based on H and the characteristic velocity $\epsilon H g k/(2\omega)$ of Eq. (22), which quantifies the numerical dissipation of the nominally inviscid solution.

4.4.2. Results

Sample particle pressure distributions at the fourth peak of the wave are shown in Fig. 21. In this view there is no discernible difference between results for the pure Lagrangian mode and enhanced free-surface particle transport velocity.

Time histories of kinetic energy are shown in Fig. 22. Dissipation is strongly dependent on resolution, with effective Reynolds number ranging from 31 for $H/\Delta x = 20$ to 959 for $H/\Delta x = 160$ with fully Lagrangian particle transport. With enhanced free-surface particle transport velocity, dissipation is slightly less, with $Re^* = 1253$ at the finest resolution.

5. Conclusions

Two new developments have been presented that enhance FVPM simulation of free-surface flows. The first is a new method to determine the ALE particle transport velocity for particles at the free surface, based on solution of a partial

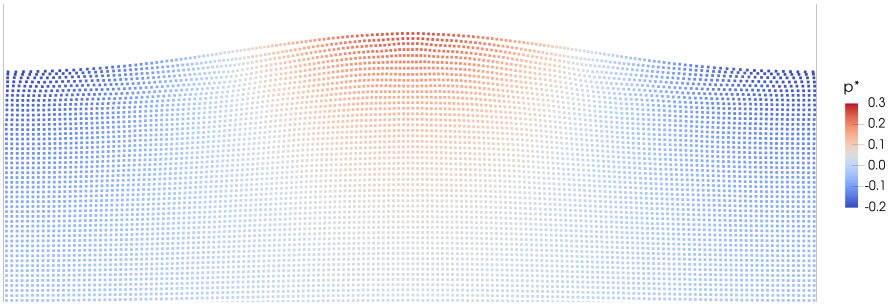

(a)

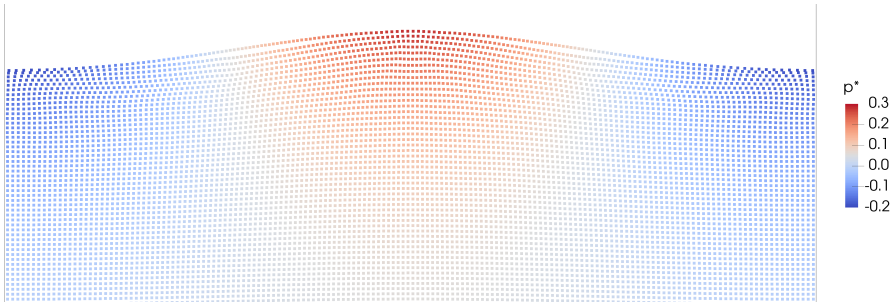

(b)

Figure 21: Dimensionless pressure $p^* = \frac{p-\rho_0 g(H-y)}{\frac{1}{2}\rho_0 U^2}$ in the standing wave test at $t^* = t/T = 4.25$ with $H/\Delta x = 160$ (a) with fully Lagrangian particle motion and (b) with enhanced free-surface particle transport velocity.

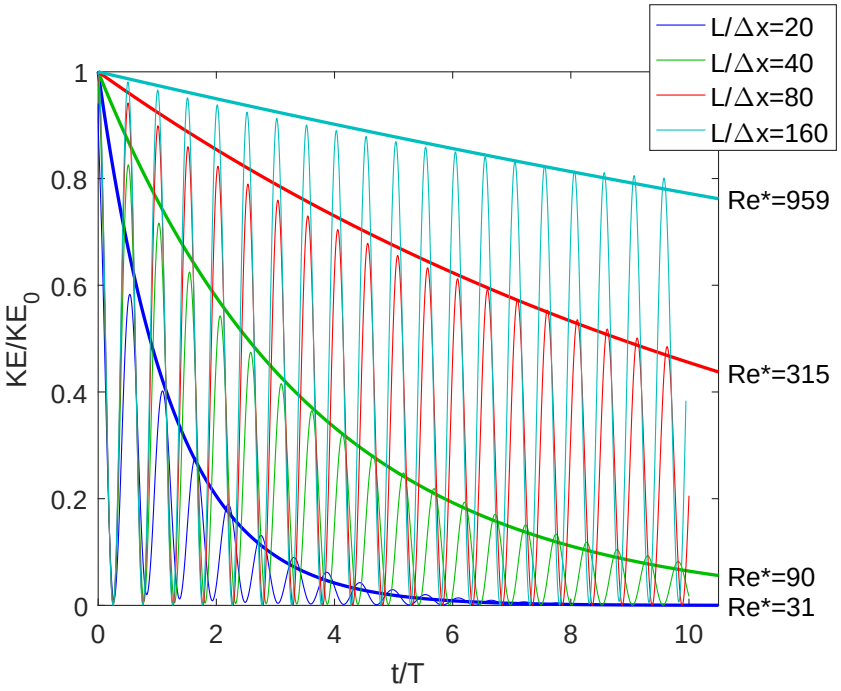

(a)

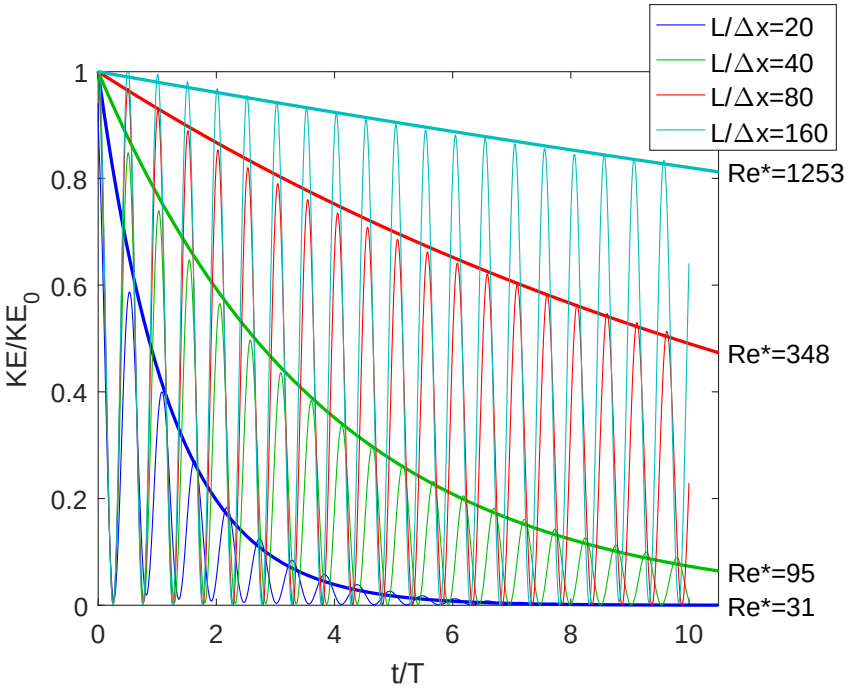

(b)

Figure 22: Kinetic energy with fitted decay curves effective Reynolds number Re^* in the standing wave test for various $H/\Delta x$ (a) with fully Lagrangian particle motion and (b) with enhanced free-surface particle transport velocity.

Riemann problem to determine the free-surface velocity consistent with zero pressure at the surface. These may be considered a form of ALE particle velocity correction (shifting), specifically adapted for the free surface, and based on an analysis of the local flow rather than a measure of uniformity or symmetry of the particle distribution. Aside from this treatment, all simulations presented here have used fully Lagrangian particle motion. The new free-surface method has been shown to improve robustness and reduce high-frequency pressure oscillations in dambreak simulations. Dambreak results show convergence and agreement against experimental data from the literature. In particular, the simulations show that the finite time taken for gate removal has a significant effect on the impact flow downstream. In simulations of a standing wave, the enhanced free-surface transport velocity formulation slightly reduces dissipation.

The second enhancement is a well-balanced formulation which enables exact equilibrium between gravity and pressure gradient. In hydrostatic tests with this formulation, normalised kinetic energy tends to machine zero. This performance is maintained with irregular geometry, and the enhanced free-surface particle transport velocity formulation, and non-uniform particles. The hydrostatic pressure distribution approaches the analytical solution with second-order convergence.

Furthermore, the dissipation and compressibility properties of FVPM have been assessed in numerical experiments on one-dimensional impact tests. FVPM with linear reconstruction shows very low dissipation, allowing acoustic waves to be preserved through many reflection cycles. Consequently, high-frequency pressure oscillations are evident in dambreak simulation, particularly with low spatial resolution. Oscillations can be suppressed by reverting to the scheme with zero-order reconstruction (introducing strong artificial dissipation), or as a preliminary test has shown, by filtering. The enhanced free-surface particle transport velocity formulation reduces high-frequency oscillations in the dambreak test. Results of standing wave simulations suggest that the new approach reduces dissipation, and its effect of reducing pressure fluctuations in the dambreak is therefore associated with better tracking of the free surface,

as intended. Collectively, this work improves the accuracy and robustness of FVPM for free surface flows.

References

[1] E. Jahanbakhsh, C. Vessaz, A. Maertens, F. Avellan, Development of a finite volume particle method for 3-D fluid flow simulations, Computer Methods in Applied Mechanics and Engineering 298 (2016) 80–107.

[2] E. Jahanbakhsh, A. Maertens, N. Quinlan, C. Vessaz, F. Avellan, Exact finite volume particle method with spherical-support kernels, Computer Methods in Applied Mechanics and Engineering.

[3] L. Lobovský, E. Botia-Vera, F. Castellana, J. Mas-Soler, A. Souto-Iglesias, Experimental investigation of dynamic pressure loads during dam break, Journal of Fluids and Structures 48 (2014) 407–434.

[4] D. Hietel, K. Steiner, J. Struckmeier, A finite volume particle method for compressible flows, Mathematical Models and Methods in Applied Science 10 (2000) 1363–1382.

[5] T. Ismagilov, Smooth volume integral conservation law and method for problems in Lagrangian coordinates, Computational Mathematics and Mathematical Physics 46 (2006) 453–464.

[6] R. Keck, D. Hietel, A projection technique for incompressible flow in the meshless finite volume particle method, Advances in Computational Mathematics 23 (2005) 143–169.

[7] M. Junk, Do finite volume methods need a mesh?, in: M. Griebel (Ed.), Meshfree Methods for Partial Differential Equations, Springer, 2003, pp. 223–238.

[8] R. Nestor, M. Basa, M. Lastiwka, N. Quinlan, Extension of the finite volume particle method to viscous flow, Journal of Computational Physics 228 (2009) 1733–1749.

[9] B. van Leer, Towards the ultimate conservative difference scheme. V - a second-order sequel to Godunov's method, Journal of Computational Physics 32 (1979) 101–136.

[10] M. Muradoglu, P. Jenny, S. B. Pope, D. A. Caughey, A consistent hybrid finite-volume/particle method for the pdf equations of turbulent reactive flows, Journal of Computational Physics 154 (2) (1999) 342 – 371. doi:https://doi.org/10.1006/jcph.1999.6316.
URL http://www.sciencedirect.com/science/article/pii/S0021999199963167

[11] A. Chertock, A. Kurganov, G. Petrova, Finite-volume-particle methods for models of transport of pollutant in shallow water, Journal of Scientific Computing 27 (1-3) (2006) 189–199. doi:10.1007/s10915-005-9060-x.
URL http://dx.doi.org/10.1007/s10915-005-9060-x

[12] S. Zhang, K. Morita, K. Fukuda, N. Shirakawa, A new algorithm for surface tension model in moving particle methods, International Journal for Numerical Methods in Fluids 55 (3) (2007) 225–240. doi:10.1002/fld.1448.
URL http://dx.doi.org/10.1002/fld.1448

[13] N. J. Quinlan, R. M. Nestor, Fast exact evaluation of particle interaction vectors in the finite volume particle method, in: M. Griebel, M. A. Schweitzer (Eds.), Meshfree Methods for Partial Differential Equations V, Vol. 79 of Lecture Notes in Computational Science and Engineering, Springer Berlin Heidelberg, 2011, pp. 219–234.

[14] N. J. Quinlan, L. Lobovskỳ, R. M. Nestor, Development of the meshless finite volume particle method with exact and efficient calculation of interparticle area, Computer Physics Communications 185 (6) (2014) 1554–1563.

[15] C. Kaland, The finite volume particle method : Recent developments and applications, Ph.D. thesis, Universität Hamburg (Dec. 2013).
URL http://ediss.sub.uni-hamburg.de/volltexte/2014/6561/

[16] N. J. Quinlan, R. M. Nestor, Fast exact evaluation of particle interaction vectors in the finite volume particle method, in: M. Griebel, M. A. Schweitzer (Eds.), Meshfree Methods for Partial Differential Equations V, Vol. 79 of Lecture Notes in Computational Science and Engineering, Springer Berlin Heidelberg, 2011, pp. 219–234. doi:10.1007/978-3-642-16229-9_14.
URL http://dx.doi.org/10.1007/978-3-642-16229-9_14

[17] D. Hietel, R. Keck, Consistency by coefficient correction in the finite volume particle method, in: M. Griebel (Ed.), Meshfree Methods for Partial Differential Equations, Lecture Notes in Computational Science and Engineering, Springer, Berlin, 2003, pp. 211–221.

[18] D. Teleaga, J. Struckmeier, A finite-volume particle method for conservation laws on moving domains, International Journal for Numerical Methods in Fluids 58 (2008) 945–967.

[19] J. Bonet, T.-S. L. Lok, Variational and momentum preservation aspects of smooth particle hydrodynamic formulations, Computer Methods in Applied Mechanics and Engineering 180 (1999) 97–115.

[20] T. Barth, D. Jespersen, The design and application of upwind schemes on unstructured meshes, in: AIAA 27th Aerospace Sciences Meeting, AIAA, Reno, 1989.

[21] M.-S. Liou, A sequel to AUSM, part II: AUSM+-up for all speeds, Journal of Computational Physics 214 (2006) 137–170.

[22] F. Dubois, Partial Riemann problem, boundary conditions, and gas dynamics, Nova Science Publishers, 2001, pp. 16–77.

[23] J.-C. Marongiu, F. Leboeuf, J. Caro, E. Parkinson, Free surface flows simulations in pelton turbines using an hybrid sph-ale method, Journal of Hydraulic Research 48 (sup1) (2010) 40–49.

doi:10.1080/00221686.2010.9641244.
URL http://dx.doi.org/10.1080/00221686.2010.9641244

[24] N. Botta, R. Klein, S. Langenberg, S. Lützenkirchen, Well balanced finite volume methods for nearly hydrostatic flows, Journal of Computational Physics 196 (2) (2004) 539–565.

[25] D. Le Touzé, A. Colagrossi, G. Colicchio, M. Greco, A critical investigation of smoothed particle hydrodynamics applied to problems with free-surfaces, Int. J. Numer. Meth. Fluids 73 (7) (2013) 660–691. doi:10.1002/fld.3819.
URL http://dx.doi.org/10.1002/fld.3819

[26] S. Marrone, A. Colagrossi, A. D. Mascio, D. L. Touz, Prediction of energy losses in water impacts using incompressible and weakly compressible models, Journal of Fluids and Structures 54 (2015) 802 – 822. doi:https://doi.org/10.1016/j.jfluidstructs.2015.01.014.
URL http://www.sciencedirect.com/science/article/pii/S0889974615000195

[27] L. Lobovský, E. Botia-Vera, F. Castellana, J. Mas-Soler, A. Souto-Iglesias, http://canal.etsin.upm.es/papers/lobovskyetaljfs2014/ (2014).

[28] A. Kiara, K. Hendrickson, D. K. P. Yue, Sph for incompressible free-surface flows. part ii: Performance of a modified sph method, Computers & Fluids 86 (2013) 510–536. doi:10.1016/j.compfluid.2013.07.016.
URL http://dx.doi.org/10.1016/j.compfluid.2013.07.016

[29] D. D. Meringolo, A. Colagrossi, S. Marrone, F. Aristodemo, On the filtering of acoustic components in weakly-compressible sph simulations, Journal of Fluids and Structures 70 (2017) 1–23. doi:10.1016/j.jfluidstructs.2017.01.005.
URL http://dx.doi.org/10.1016/j.jfluidstructs.2017.01.005

[30] J. L. Cercos-Pita, AQUAgpusph, a new free 3D SPH solver accelerated with OpenCL, Computer Physics Communications 192 (2015) 295–312.

[31] J. M. Gimenez, L. M. González, An extended validation of the last generation of particle finite element method for free surface flows, Journal of Computational Physics 284 (2015) 186–205.

[32] A. Colagrossi, M. Landrini, Numerical simulation of interfacial flows by smoothed particle hydrodynamics, Journal of Computational Physics 191 (2) (2003) 448–475.

[33] P. K. Stansby, A. Chegini, T. C. D. Barnes, The initial stages of dam-break flow, Journal of Fluid Mechanics 374 (1998) 407–424. doi:10.1017/s0022112098001918.
URL http://dx.doi.org/10.1017/s0022112098001918

[34] M. Antuono, A. Colagrossi, S. Marrone, C. Lugni, Propagation of gravity waves through an sph scheme with numerical diffusive terms, Computer Physics Communications 182 (4) (2011) 866–877.

[35] J. Lighthill, M. Lighthill, Waves in fluids, Cambridge University Press, 2001.